Relationship between sprite current and morphology

L. Contreras-Vidal[1], R. Sonnenfeld[1], C. da Silva[1], M. McHarg[2], D. Jensen[1], J. Harley[2], L. Taylor[2], R. Haaland[3], H. Stenbaek-Nielsen[4]

[1]Department of Physics and Langmuir Laboratory, New Mexico Tech, Socorro, NM
[2]Department of Physics, U.S. Air Force Academy, Colorado Springs, CO
[3]Augsburg University, Minneapolis, MN
[4]University of Alaska Fairbanks, Geophysical Institute, Fairbanks, AK

Key Points:

- Optically-large sprites with upward streamers (carrots and jellyfish) tend to have larger sprite current moments than column sprites
- 63 sprites were detected using up to 100,000 fps high-speed video. VLF remote sensing shows that 56% of them have a sprite current signature
- Several vigorously-luminous sprites have remarkably large peak current moments, up to 2,700 kA km

Corresponding author: Caitano L. da Silva, `caitano.dasilva@nmt.edu`

Abstract

On June 2nd and 3rd, 2019, 63 sprites were captured from Langmuir Laboratory in central New Mexico. The two storms investigated were located in northwest Texas, 400–800 km away from the observation site. Optical recordings were made with a Phantom V2010 camera operating at up to 100,000 frames per second. Electromagnetic remote sensing of lightning and sprite electric fields was performed with a sensitive slow antenna (LEFA). Data from the Earth Networks Total Lightning Network (ENTLN) were used to locate the sprite parent flashes. The combined information of these three data sets reveals that a staggering fraction of more than half of the sprites observed have a distinguishable electromagnetic signature attributed to currents flowing within the sprite body. Furthermore, these sprite current signatures were unusually large in comparison to previous reports. The sprite electric field changes have roughly half the amplitude of their parent lightning flash's, corresponding to sprite peak currents of 26–58 kA on average. The largest sprites have current moments of up to 2,700 kA km, as inferred from a computationally-efficient method to solve Maxwell's equations. Detailed comparison between the sprites' electromagnetic signatures and high-speed optical recordings show that optically-large sprites containing upward streamers (carrots and jellyfish) tend to have larger electrical currents than the ones displaying only downward streamer development (column sprites). Finally, a clear increasing trend in peak current moment is evident with increasing morphological complexity, from columns to carrots to jellyfish sprites.

1 Introduction

Sprites consist of large scale electrical discharges taking place in the mesosphere, near the edge of space. They are triggered by quasi-electrostatic fields typically generated by positive cloud-to-ground lightning in underlying thunderstorms (Boccippio et al., 1995; da Silva & São Sabbas, 2013; Luque & Ebert, 2010; Pasko et al., 1997; Pasko, 2010). Since their discovery 30 years ago (Franz et al., 1990; Sentman et al., 1995), sprites have been extensively studied for their impact on mesospheric chemistry and their potential as a tool for remote sensing of the mesosphere-lower ionosphere interface, a region which is difficult to access by conventional observation techniques. In that time, researchers have remotely observed sprites optical, electromagnetic (EM), and acoustic signatures. They have learned that certain sprites display an EM signature characteristic of a vertical current (Cummer, 2003; Pasko et al., 1998). However, measurements of sprite currents remain scant in the literature.

Figure 1a shows an example of a Very Low Frequency (VLF) signature of a jellyfish sprite and its parent flash, observed on June 3rd, 2019. The return stroke radio signal detected by the Earth Networks Total Lightning Network (ENTLN) and by a slow antenna from the Langmuir Electric Field Array (LEFA) (Sonnenfeld & Hager, 2013) starts at t=0. The second pulse at $t = 8.97$ ms is the EM signature of sprite currents. Figure 1 also shows the relationship between the sprite electromagnetic signature and optical integrated luminosity (1b) and high-speed imagery (1c–1g). This is a key figure in this manuscript and is described in detail in the Results section. The conceptual idea is that sprite streamers traversing the mesosphere (mostly downward) displace electrical charge (mostly concentrated at streamer heads). The resulting electrical current (I) is changing over time and space, emitting EM radiation that can be detected on the ground with electric (e.g., Sonnenfeld & Hager, 2013) or magnetic (e.g., Cummer, 2003) field sensors. The strength of this electromagnetic radiation is directly proportional to the current moment (M_I), defined as the integral of the current over the vertical spatial direction. The current moment required to produce the sprite EM signature shown in Figure 1a is shown in Figure 1b, as a red line with values in the right-hand-side vertical axis.

Reising et al. (1999) and Cummer et al. (1998) presented the first experimental evidence that current flowing in a sprite produces low frequency radiation. They inferred

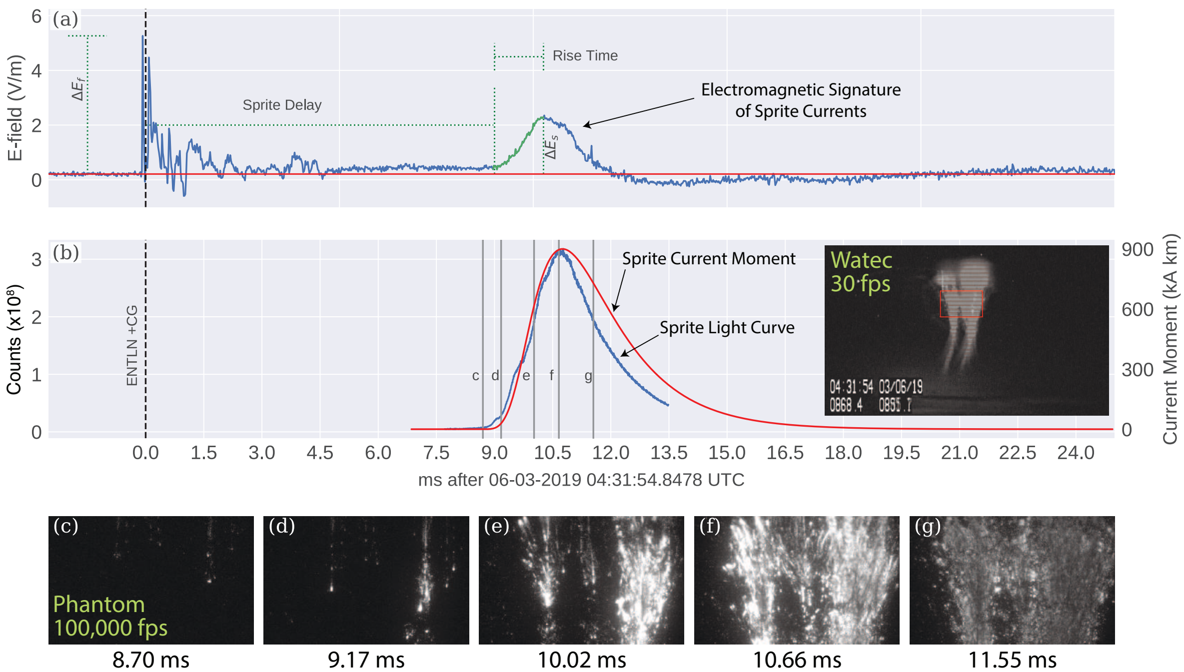

Figure 1. A jellyfish sprite detected from Langmuir Lab in Central New Mexico, USA, on June 3, 2019. (a) E-field from parent flash and sprite. The vertical black dashed line marks the occurrence time of the parent +CG detected by ENTLN. (b) High-speed video integrated brightness (blue line with vertical axis on the left), and extracted sprite current moment (red line with magnitude shown in the right-hand side axis). The inset in panel (b) shows the Watec camera capture, and the red rectangle shows the Phantom camera field of view. (c-g) Selected high-speed video frames captured with the Phantom camera. Frames are represented in panel (b) as vertical lines. Full video is available at (Contreras-Vidal et al., 2020).

the causal relationship between the sprite current signature and the sprite by showing that the peaks in the observed ELF waveforms occurring some milliseconds after the initial VLF sferic signal were coincident with the sprite integrated optical brightness. Our Figure 1b shows the same clear relationship between optical signature and ELF waveform reported by Cummer et al. (1998). This unique feature allows for the detection of sprites from their radio signals without a video camera. Stanley et al. (2000) reported the detection of 11 day-time sprites during a period of 3 days using the sprite current radio-signature.

EM signatures of sprite currents have been used for different quantitative and qualitative studies of sprites. Cummer and Stanley (1999) analyzed synchronized high-speed video images and ELF-VLF radio emissions from 11 sprite clusters observed in October of 1997. Their quantitative analysis showed that vertical lightning charge moment changes of 150–1100 C km, occurred before the optical emissions reached their peak with delays of 2–11 ms from the lightning discharge. Cummer (2003) obtained maximum values of sprite current-moment amplitudes of $\sim$1000 kA km from 76 sprites during a period of 17 days.

Hu et al. (2002) reported sprite current moments of the order of 500 kA km. They also showed that sprites with current signatures are produced by positive cloud-to-ground (CG) flashes that have larger charge moment changes than the ones that do not have a current signature. Li and Cummer (2011) reported sprite current moments of less than

Table 1. Sprite current-moment estimates in previous investigations and in the present paper.

Source		Peak current moment (kA km)
Previous Work		
Cummer et al. (1998)		100-200
Cummer and Stanley (1999)		~400
Cummer and Fllekrug (2001)		60-80
Hu et al. (2002)		~500
Cummer (2003)		Up to ~1,000
Cummer, Jaugey, et al. (2006)		190-320
Hu et al. (2007)		~400
Li et al. (2008)		50-100
Gamerota et al. (2011)		30-80
Li and Cummer (2011)		80
Lu et al. (2013)		160
This Work	Detections out of total	Avg. $\pm$ Std. dev. (kA km)
All data	35 out of 63	1,237 $\pm$ 939
Column sprites	7 out of 15	266 $\pm$ 66
Carrots	11 out of 30	1,066 $\pm$ 898
Jellyfish	10 out of 10	1,828 $\pm$ 744
Undetermined	7 out of 8	1,295 $\pm$ 937

~400 kA km. Soula et al. (2015) reported that long-delayed sprites are associated with current-moment waveforms of low amplitude and long duration. Sonnenfeld and Hager (2013) used electric field data from a sprite to model the electric field associated with its current, estimating the sprite peak current to be 18 kA (current, not current-moment). A summary of sprite current-moment estimates reported in the peer-reviewed literature can be found in (the top part of) Table 1. In this manuscript we focus on providing estimates of peak current and peak current moment of the sprite itself, and not of its parent lightning. This objective contrasts with the one from most articles on this subject, where the main objective is to report on the charge-moment change of sprite-producing lightning (e.g., Hu et al., 2002).

In this study, we present a detailed characterization and statistical analysis of optical and electric field measurements of 63 sprites and their parent flashes. The sprites were observed during the nights of June 2 and 3, 2019 above storms in northwest Texas (as described in Section 2.1). These two storms prolifically produced sprites with current signatures. Using this extensive data set, augmented with computer simulations (Section 2.2), we report the statistical properties of these electromagnetic signatures, including peak currents, peak current moments, and sprite delays (Section 3.2). Detailed comparison between optical and electromagnetic signatures reveals that optically-large sprites also have large peak current moments, up to 2,700 kA km. Finally, our analysis reveals a clear increasing trend in peak current moment with increasing morphological complexity, from columns to carrots to jellyfish sprites (Section 3.3).

2 Methodology

2.1 Instruments and Data Sets

Sprite observations were carried out from the Langmuir Laboratory for Atmospheric Research, a mountain-top facility at 3.3 km altitude above sea level located in central

New Mexico (34.06° N, 106.90° W). The EM signature in Figure 1a was recorded with the sensitive channel of one of the slow antennas from Langmuir Lab's LEFA array (this antenna is located 25 km east of the lab). Slow-antennas measure electric field changes on time scales less than a high-pass time constant. The time constant of the sensors used here is 0.1592 s and the low-pass cutoff frequency is 24.1 kHz (Hager et al., 2012). The three-channel design of the LEFA slow antenna extends the dynamic range of electrostatic field change measurements from 0.021 V/m to 496 kV/m. The data-acquisition-module is set to 50 kS/s sustained sampling rate, which covers the range of time-scales of the electrostatic processes in lightning (Zhang, 2010; Hager et al., 2012). Calibration of LEFA is described in detail by Hager et al. (2012). Insights on the validity of the instrument's calibration are given in Section 3.1.

Classification, location, peak current and timing of the parent flashes were obtained from the ENTLN. ENTLN is a global lighting detection network that has been operational since 2009. The ENTLN sensors are broadband electric field sensors that detect both intra-cloud (IC) and cloud-to-ground (CG) lightning and provide timing, location, classification, and peak current measurements. Evaluation of ENTLN performance results have shown a total flash detection efficiency of 97.5% and classification accuracy of 91% for CG flashes (Lapierre, 2019). The median values of location error and absolute peak current estimation error of ENTLN have been reported to be 215 m and 15% respectively by using cloud-to-ground (CG) lightning data acquired at the Lightning Observatory in Gainesville as ground truth and rocket-triggered lightning data obtained at Camp Blanding, Florida (Zhu et al., 2017).

Every ENTLN-identified positive cloud-to-ground (CG) flash in a radius of 100 km from the observed storm was synchronized with LEFA data and integrated optical brightness from the high-speed video, as shown Figure 1. LEFA data and integrated optical brightness are corrected for transmission delays. Through LEFA, we were able to quantify key characteristics of the radiated electromagnetic field, such as the electric field change generated by a sprite (ΔE_s) and its parent flash (ΔE_f). We also determine the 10–90% rise time of the sprite signal, and its delay from the parent flash. The electric field changes are measured with respect to the average electric field value in a 2.5-ms window preceding the parent flash, and the sprite delay is measured with respect to the ENTLN-reported time of the parent flash. The peak current of the parent flash as reported by ENTLN was accepted as correct. Figure 1a illustrates how these waveform features are defined.

On June 2, 2019, 363 +CG flashes were registered between 03:00 and 08:00 UTC near the border of Texas and Oklahoma. Positive-polarity flashes account for 6.8% of the total CG strikes in that thunderstorm. We detected sprites produced by 33 (9%) of the +CG flashes by either video, LEFA, or both. Sixteen of these events showed a characteristic sprite signature in the LEFA data. The parent CG flashes were located at an average distance of 690 km from Langmuir Lab, as shown in Figure 2. On the following night, June 3, 113 +CG flashes were registered between 04:00 and 06:10 UTC in northwest Texas. Positive-polarity CGs account for 1.1% of the total CG flashes in that storm. We detected sprites produced by 30 (27%) of the +CGs. Nineteen of these events showed a characteristic EM sprite signature. The parent +CGs were located at an average distance of 465 km from Langmuir Lab, as also shown in Figure 2. All sprites reported in this paper have been produced by +CGs, and for the purposes of electric field range normalization and temporal synchronization we assume the sprite geographical location to be the same as of its parent flash.

Optical observations were made from the Langmuir Lab in central NM of sprites taking place over storms in northwest Texas, approximately 400–800 km away, as shown in Figure 2. Optical recordings were made with a 4-megapixel Phantom V2640 high-speed video camera operating at up to 100,000 frames per second (fps) and with a Watec 902H2 camera operating at 30 fps. The Phantom data are used to produce light curves of the observed sprites, such as the one shown in Figure 1b. The light curve is simply defined

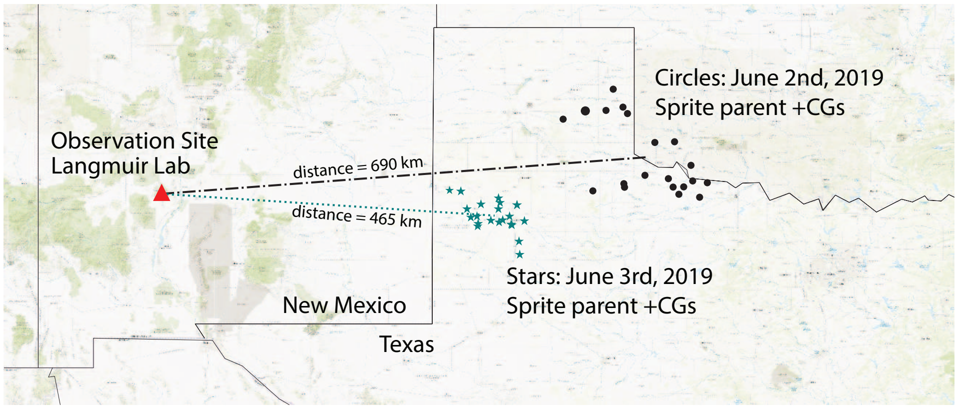

Figure 2. Map showing the location of sprite parent flashes detected by ENTLN during both nights of observations.

as the visible brightness integrated over the camera's field of view. Figures 1c to 1g show example image frames extracted from the high-speed video. In this particular example, downward streamers start to appear 8.7 ms after the parent CG (frame c). At 9.17 ms (frame d), the sprite element on the right increased brightness and a second sprite element has been initiated on the left-hand side of the frame. After 10.02 ms (frame e), three sprite carrots can be identified in the field of view, with clear upward streamer development, along with an overall increase in sprite brightness. Peak brightness was reached at 10.66 ms after its parent flash (frame f), followed by uniform decay in luminosity (frame g). The inset in Figure 1b shows the same sprite as captured by the Watec camera. The Phantom camera field of view is marked in this figure as a red rectangle.

Recordings from both the Phantom and Watec cameras are used to produce morphological classification of the sprites detected (Stenbaek-Nielsen & McHarg, 2008). We classify the 63 sprites into four morphological categories: columns (15), carrots (30), jellyfish (10), and undetermined (8). Column sprites are the ones that present downward streamers only (or at least predominantly). Carrot sprites, on the other hand, present both downward and upward streamers (Stenbaek-Nielsen & McHarg, 2008). Jellyfish are large, short-lived sprites comprised of many carrots and columns in a small geographic area so they appear in the Watec images as one large sprite. As seen from our high-speed videos, they tend to last 8 ms or less. The undetermined category contains 7 sprites that were solely detected based on their electromagnetic signature (and thus they took place outside the field of view of our cameras) and 1 sprite that was too distant to be classified (it appeared as a glare in the Phantom camera, and it was not detected by the Watec or even by LEFA).

Both storms studied here were identified as Mesoscale Convective Systems (MCS) with a trailing stratiform configuration (Soula et al., 2009). Most of the sprites were produced while the stratiform area was clearly developed and during periods of substantial increase of rainfall in regions with radar reflectivity between 25 and 35 dBZ. Figure 3 shows NEXRAD Level-III radar composite imagery for both storms overlaid with the location of sprite parent-flashes in the appropriate time window. Figures 3a–3c (June 2) capture 40 minute snapshots of storm evolution. The overlaid flashes occur between 20 minutes before and 20 minutes after the labeled panel time. Figures 3d–3f (June 3) show evolution of the latter storm, but the snapshots are separated by 105 minutes. Complete videos of the radar imagery, as well as all data used in this paper, are available at (Contreras-Vidal et al., 2020).

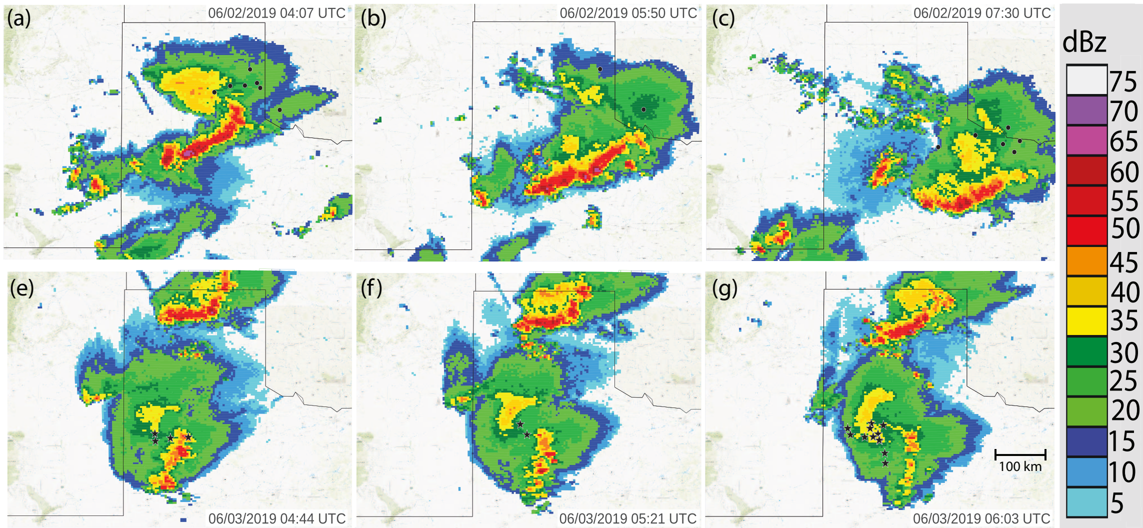

Figure 3. NEXRAD Level-III radar composite imagery for both storms and location of sprite parent flashes. Panel (a) to (c) correspond to the storm on June 2 where the sprite parent flashes are represented as black dots. Panel (d) to (f) correspond to the storm on June 3 where the sprite parent flashes are represented as black stars.

2.2 Modeling Strategy for Extracting the Source Current Parameters

It is common practice to represent the electromagnetic field emitted by a lightning return stroke as an approximate solution to a current pulse traveling on a transmission line (Orville, 1991; Rakov & Uman, 1998; Uman & McLain, 1969). The predicted magnitude of the electric field change (ΔE_f) is linearly proportional to the return stroke peak current (I_p):

$$\Delta E_f = \frac{v}{2\pi\varepsilon_0 c^2 D} I_p \tag{1}$$

where D is the source-observer distance, v is the return stroke speed, c is the speed of light, and ε_0 is the dielectric permittivity of free space. This solution is valid in the far-field regime only. It has been showed by a number of authors that equation (1) can reasonably model the observed relationship between ΔE_f and I_p (e.g., Nag et al., 2014; Orville, 1991). In Section 3.1, we discuss how well equation (1) applies to our data set.

When modeling the electromagnetic signature of sprites, a more general expression for the electric field needs to be used, which does not employ a far-field approximation, and accounts for the effect of additional ionospheric and ground reflections (Hager et al., 2012; Sonnenfeld & Hager, 2013). In more general terms, the vertical electric field just above the surface of a perfectly-conducting ground, at plane distance D from the source, can be conveniently expressed as a sum of three components, derived from an integral solution to the Maxwell's equations:

$$E(t) = \sum_{i=1}^{N} \frac{s_I^{i+1}}{2\pi\varepsilon_0} \left\{ \frac{(2-3\sin^2\theta_i)}{R_i^3} M_Q(t_i') + \frac{(2-3\sin^2\theta_i)}{cR_i^2} M_I(t_i') - \frac{\sin^2\theta_i}{c^2 R_i} \frac{dM_I(t_i')}{dt} \right\} \tag{2}$$

where M_Q is the charge moment change, $M_I = dM_Q/dt$ is the current moment, $R_i = \sqrt{h_i^2 + D^2}$ is the source-observer distance, $\sin\theta_i = D/R_i$, $t_i' = t - R_i/c$ is the retarded time, s_I indicates the direction (or sign) of current propagation ($+1 =$ upward, $-1 =$ downward), ε_0 is the vacuum electric permittivity, $N \to \infty$ is the number of images, and c is the speed of light. For a distributed source current $I(z,t)$, as function of height z and time t, the current moment can be obtained as $M_I(t) = \int I(z,t)dz$.

If we reduce the summation above to a single term ($N=1$), equation (2) describes the electric field produced by a source at height h_1 above a perfectly-conducting ground plane and its image. This equation is a simplification of Uman's derivation, commonly used for simulation of lightning electromagnetic fields (Uman et al., 1975) if the source is small in comparison to the source-observer distance (da Silva & Pasko, 2015, equations (7)-(10)). The three terms inside the curly brackets are commonly referred to as the electrostatic, induction, and radiation components of the total electric field, respectively. For distances far away from the source the radiation term dominates because of its weaker dependence on the source-observer distance, giving rise to equation (1). For this reason, the electric field changes reported here are range-normalized by a D_n/D factor, as it is common practice for lightning detection systems (Orville, 1991). We use here $D_\mathrm{n} = 500$ km. Extending equation (2) to an infinite summation ($N \to \infty$), allows one to account for the effects of image sources in the ionosphere (Hager et al., 2012; Sonnenfeld & Hager, 2013), modeled as a perfect conductor at a height H above ground. This is done by realizing that every ionospheric image produces a subsequent image on the ground and so on, creating an infinite set of image currents. The effective source heights for these image currents are $h_i = iH - h_1$ if i is even or $h_i = (i-1)H + h_1$ if i is odd.

In this study, we use equation (2) to retrieve the sprite current moments. The current moment is produced by a current pulse propagating downward from 80 to 70 km altitude at a speed of 10^7 m/s, which is of the order of magnitude of observed sprite streamer velocities (Stenbaek-Nielsen & McHarg, 2008). The current pulse shape is described by a Heidler (1985) function, which has a sharp rise and a slower fall following exponential functions of time. The current pulse amplitude varies as a function of distance according to a smooth Gaussian function, referred to as the modified transmission line Gaussian (MTLG) model (da Silva et al., 2016, equation (7)). The current pulse risetime and falltime are empirically adjusted to fit the recorded sprite sferic. The approach is validated by comparison with the full solution obtained from a two-dimensional FDTD simulation code (Marshall, 2012; Marshall et al., 2015). The FDTD simulations are made in spherical coordinates, accounting for Earth's curvature. The ground is represented as a perfect conductor, and the ionosphere is represented as a cold plasma according to a Wait and Spies (1964) electron density profile suitable for the nighttime ionosphere at midlatitudes. Figure 4 shows the simulated electric field for the sprite shown in Figure 1. Figure 4a shows excellent agreement between equation (2) and the FDTD simulation, while Figure 4b shows the contribution of the three terms in equation (2) to the total electric field.

Equation (2) allows one to extract the source current moment without any ambiguities, and is practically independent of the chosen source radiator length. From that one can estimate the peak source current by dividing the extracted peak current moment by the effective radiator length. For the MTLG model, the effective radiator length is 1/3 of the actual channel length (da Silva et al., 2016, equation (9)). In Section 3.2 below, when estimating peak currents from equation (2), we assume the total sprite length to be 50 km.

3 Results

3.1 Verification of LEFA's Calibration

The calibration of electric-field instruments is not trivial. The electronic gain of a slow antenna is easy to calculate, and a flat-plate placed on the ground can be assumed to be measuring "true field". However, the moment the ground is not flat, or the instrument is placed on a stand, both the local topography and the stand design change the

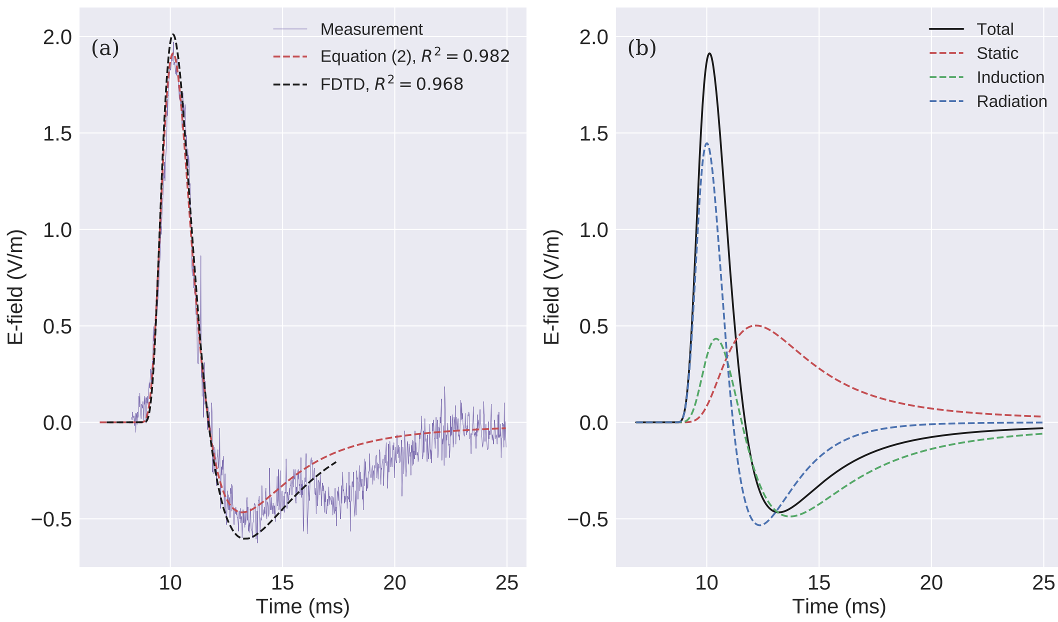

Figure 4. (a) Comparison between measured sferic, simulated with equation (2), and simulated via the FDTD technique for the sprite shown in Figure 1 (the source current moment is shown in Figure 1b). (b) The static, induction, and radiation components of the total electric field according to equation (2).

instrument sensitivity. LEFA was originally calibrated by side-by-side measurements with a previously calibrated field-mill. After that, inter-site calibration factors were calculated by comparing measurements obtained on over 800 distant ($D >$100 km) lightning flashes (Hager et al., 2012). Nonetheless, it is worthwhile to see if the wealth of data collected in this study can confirm our prior calibrations.

During the two consecutive nights studied, 14,004 CG flashes were recorded; 96.6% percent were of negative polarity, while the remaining 3.4% were positive. Figure 5 shows the relationship between the measured electric field change with LEFA (based on prior calibration described above) and the peak current reported by ENTLN. The electric field has been normalized by D/D_n, where D is the distance of the flash from Langmuir Lab and $D_n = 500$ km is a reference distance. It can be seen that both polarities present an approximately linear relationship between ΔE_f and I_p. Nag et al. (2014) showed that equation (1) can capture the relationship between ΔE_f measured by a flat-plate antenna (with uniform response between 16 Hz and 10 MHz) and the peak current reported by the National Lightning Detection Network, if one assumes $v = 0.6c$. This result is shown in Figure 5a alongside the derived linear fit for our LEFA–ENTLN data set. The difference in slope between the two curves is under 20%. Figure 5a shows that our system's calibration works well for lightning return strokes, in agreement with previous work in the literature. More importantly, the agreement of Figure 5a with the literature shows that our system *does not* overestimate the inferred lightning (or sprite) current properties. Figure 5b shows that the relationship between ΔE_f and I_p for +CG flashes is not as well represented by a linear dependence as it is for −CGs (see the lower value for the coefficient of determination of the linear fit in the figure legend). This conclusion is in agreement with the findings of Nag et al. (2014).

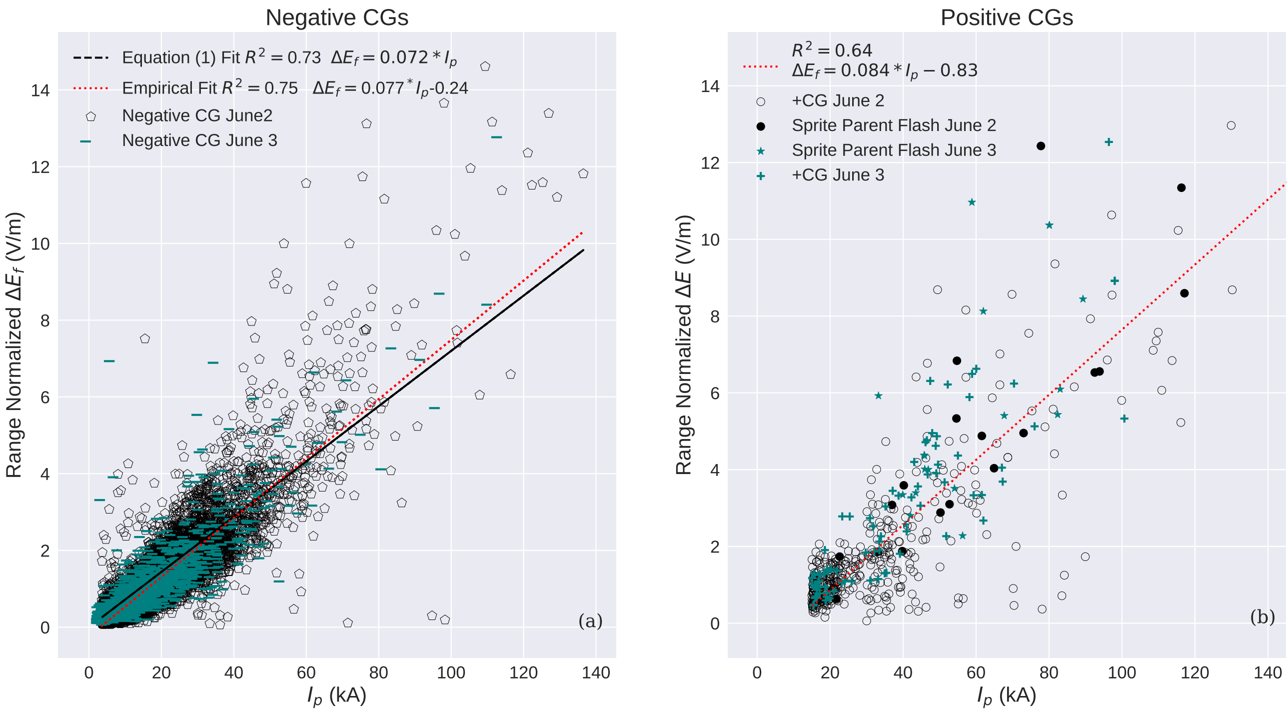

Figure 5. Electric field change (ΔE_f) detected by LEFA versus peak electrical current (I_p) provided by ENTLN for all positive (a) and negative (b) CG flashes in the two storms investigated. The electric field change is range-normalized to 500 km.

3.2 Inferred Sprite Electromagnetic Properties

During the two observation nights 63 sprites were detected. Thirty five of them had a sprite current signature (56%). This extensive data set is fully available online for the reader's reference (Contreras-Vidal et al., 2020). The fraction we report here contrasts with previous work by Cummer (2003), who reported a fraction of 10% sprite current signatures based on Extreme Low Frequencies (ELF) radiation observations (Cummer, Frey, et al., 2006). Among the 35 sprite current signatures detected there are seven (20%) cases were no associated optical signals were detected by either of the cameras, similarly to the findings by Stanley et al. (2000). The median risetime of the detected sprite electric field signatures is 1.09 ms with a standard deviation of 0.45 ms.

The average peak current of sprite-parent flashes is 69.3 kA as measured by the ENTLN network. In addition, the average values for ΔE_f and ΔE_s are 6.79 V/m and 3.08 V/m respectively, where ΔE_s and ΔE_f are the range-normalized magnitudes of the electric field changes of the sprite and the flash (Figure 1a), making ΔE_s nearly half of ΔE_f. Sprite delays were determined exclusively from the EM signature, as illustrated in Figure 1a. The obtained statistical distribution is shown in Figure 6. Most of the observed sprites have short delays ranging between 0.14 ms and 8.97 ms, with a median value of 2.15 ms. Typical delays have been reported before to be less than 5 ms (Li et al., 2008).

The same authors define long-delayed sprites as the ones that initiate more than 10 ms after the parent return stroke, with delays ranging between 10 and 290 ms. In Figure 6 we have one event in the latter category, with a delay of 133 ms.

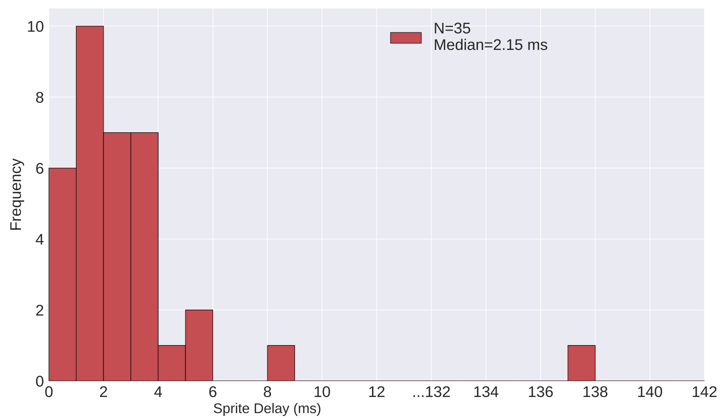

Figure 6. Distribution of sprite delays measured from the sprite electromagnetic signature.

Repurposing equation (1) $\Delta E_s = 0.072 I_p$, with ΔE_s being the electric field change of the sprite and I_p in units of kA, we can obtain a distribution of empirically-determined sprite currents, as shown Figure 7a. The minimum and maximum values of the sprite currents calculated here are 7.8 kA and 123.06 kA, while the median value is 26.08 kA which is close to the value estimated by Cummer (2003). This simple estimate using equation (1) assumes that the peak current is simply proportional to the range-normalized electric field change, with no correction to the size of the electromagnetic radiator. It essentially only uses the information regarding the peak of the electric field change waveform. Now we proceed to estimate the source current magnitude by using the full electric field change waveform by means of equation (2), and to compare both methods. The comparison is shown in Figure 7b and discussed below.

Figure 1b shows the extracted current moment for the sprite sferic shown in Figure 1a using equation (2). Figure 4a shows a comparison between measured and simulated electric field change waveforms for the same sprite. The quality of fit is assured by the high value for the coefficient of determination between simulation and data, $R^2 = 0.982$. Figure 4a shows not only that equation (2) can match the observations, but that it is also virtually equivalent to the result yielded by a FDTD simulation accounting for Earth's curvature (Marshall, 2012). Figure 4b shows the contributions of the three terms between the curly brackets in equation (2) to the total electric field, illustrating that although the radiation component is dominant, the other two components are significant. In fact, our simulations indicate that the current moment shown in Figure 1b produces an electric field change that varies with distance as $\propto (D_n/D)^{0.46}$ for distances between 300 km and 600 km.

Figure 8 shows the distribution of peak current moments extracted from the 28 waveforms for which a good fit between simulation and measurement could be obtained, i.e., for $R^2 > 0.7$, as shown in the right-hand side vertical axis. The median peak current moment inferred here is 1,116 kA km, while the maximum is 2,742 kA km, which is more than twice as large in magnitude to the highest value previously reported in the peer-reviewed literature ∼1000 kA km (Cummer, 2003). The minimum magnitude detected was 152 kA km which is similar in magnitude to the value inferred by Lu et al. (2013)

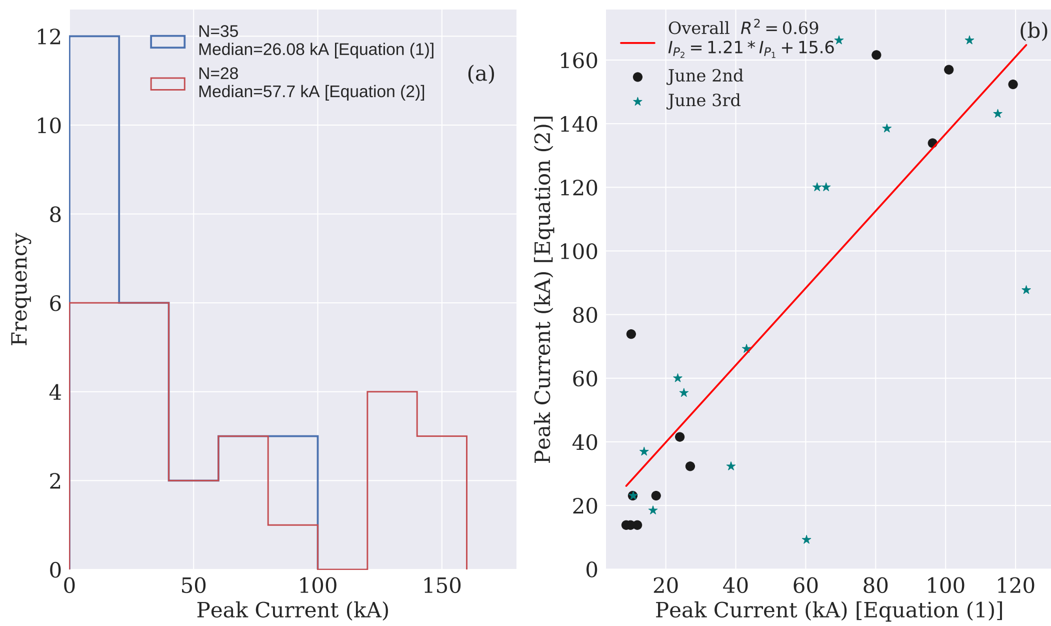

Figure 7. (a) Distribution of sprite peak currents calculated using equations (1) and (2). (b) Direct comparison between the two methods to estimate sprite peak current. When using equation (2), we assume the total sprite length to be 50 km. The different symbols correspond to the two nights of observations.

and to several other reports listed in Table 1. Sprite electric field signatures as low $\Delta E_s = 0.1$ V/m (range normalized to 500 km) can be easily detected by LEFA. This value is 5 times greater than the lowest electric field value that LEFA can resolve (see Section 2.1). This value corresponds approximately to peak current moments of the order of 50 kA km, meaning that we could have identified current moments of the order of tens of kA km if present.

Additionally, note that all fits yielding values >2,000 kA km in Figure 8 are obtained with a high-level of fit accuracy (all with $R^2 > 0.9$, with the exception of only one with $R^2 > 0.75$). This fact gives us confidence to state that the sprite signatures reported here correspond to some of the strongest sprite current moments ever measured. Simulations were performed assuming that a sprite may be better-represent by a longer electromagnetic radiator, extending from 80 km altitude down to 60 km or 50 km. The extracted peak current moment did not vary significantly when the length of the radiator was changed. The quantity current moment (rather than current) is preferred here because it is not affected by the ambiguities involved in evaluating the electric field radiated by a source that is small in comparison to the source-observer distance (da Silva et al., 2016).

The peak current moments shown in Figure 8 can be converted into peak currents by assuming a specific length for the electromagnetic radiator (see Section 2.2). Assuming a sprite length of 50 km, we obtain the peak current distribution shown in Figure 7a. The minimum and maximum values of the sprite peak currents calculated with this method are 9.23 kA and 166.2 kA, while the median value is 57.7 kA which is twice as large in magnitude to the value estimated using equation (1). The distribution of peak current moments obtained with equation (2) is different than the distribution of peak currents obtained by equation (1). The latter is equivalent to the distribution of range-

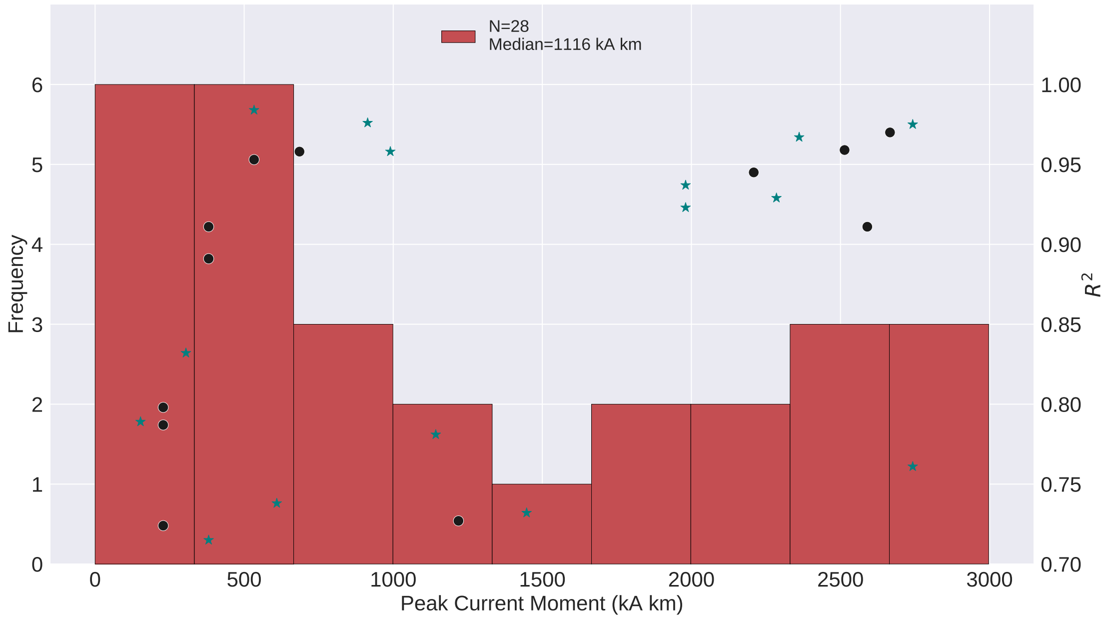

Figure 8. Distribution of peak current moments (left-hand-side vertical axis) and corresponding coefficient of determination (right axis) used as a quality-of-fit metric between simulated and measured electric field waveforms. Similarly to Figure 7b, the different symbols correspond to the two nights of observations. This figure excludes 7 sprites for which an electric field change signature is available, but a reasonably-accurate simulation fit was not possible.

normalized electric field changes. The distribution obtained with equation (2) does not present a monotonic decrease as a function of peak current, it actually has a secondary peak at ~150 kA.

Figure 7b shows the relation between the calculated peak current using both methods. The figure shows that the two quantities are not precisely linearly proportional ($R^2 = 0.69$), and also that a linear fit between the two yields a large constant offset (>15 kA), demonstrating the need to precisely fit the electric change waveform when estimating the source current parameters, and making the peak current estimates using equation (1) in Figure 7a not as accurate as those derived from equation (2). The discrepancy happens largely because equation (1) has been validated for lightning return strokes, but sprite waveforms have very different risetimes — ~1 μs for lightning versus ~1 ms for sprites. Another contributing effect is that the sprite E-field signature is largely affected by ionospheric reflections, because the radiation source is very close to the ionosphere.

3.3 Relationship Between Optical and Electromagnetic Signatures

Comparison between video and E-field measurements is summarized in Figure 9 and in the bottom part of Table 1. Figure 9 shows the peak current moment as a function of the optical morphological classification. The figure shows that sprite peak current moment increases with morphological complexity, from columns to carrots to jellyfish. From Figure 9a we can see that all column sprites have peak current moments under 400 kA km, and also that a large fraction of the columns and carrots do not have

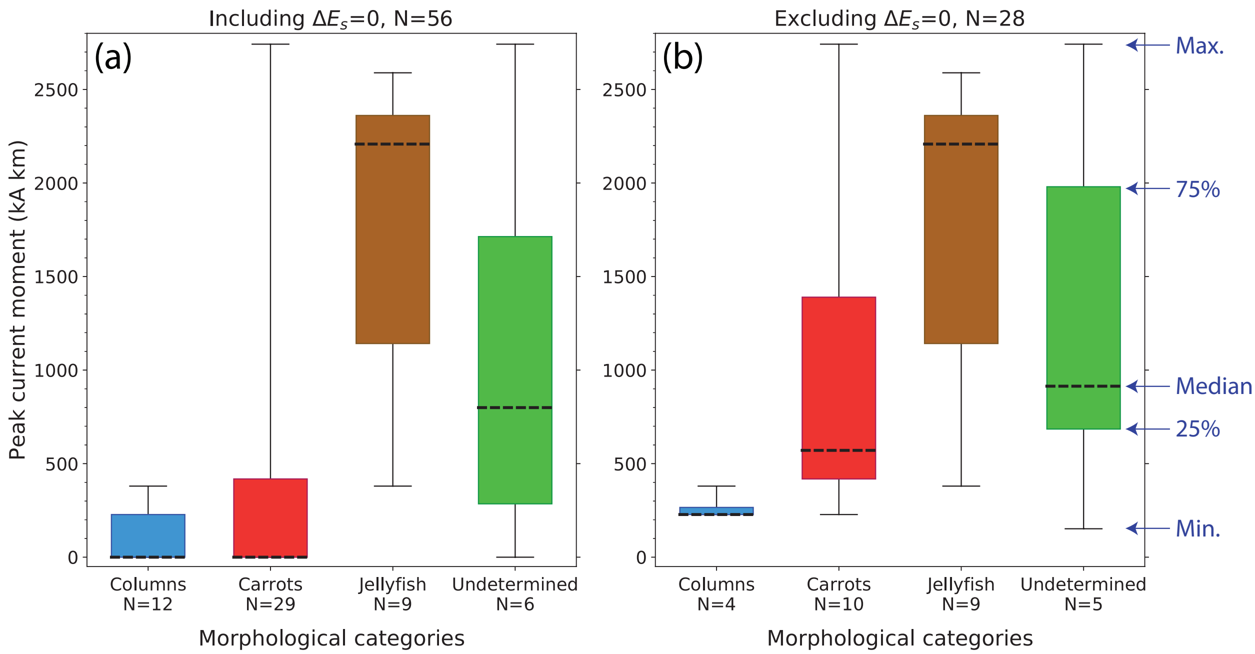

Figure 9. Box plot of extracted peak current moment as a function of sprite morphological classification. Panel (a) includes the cases for which no sprite electric field change was detected. These cases are counted as zero current moment. Panel (b) shows only the cases for which a signature was detected and a good fit between simulation and model could be made. Similarly to Figure 8, both panels exclude 7 sprites for which an electric field change signature is available, but a reasonably-accurate simulation fit was not possible. The undetermined category contains mostly sprites that have an EM signature, but their corresponding optical emissions took place outside of the camera's field-of-view.

an associated electric field change making the minimum, 25 percentile, and median all coincide at 0 kA km value. In Figure 9b we repeat the analysis from 9a, but excluding the $\Delta E_s = 0$ cases. The increasing median peak current moment (from left to right) is now more evident in Figure 9b. It is also easy to see (comparing the number of samples, N, in the horizontal axis labels) that all jellyfish sprites detected have a sprite current signature. Please note that these numbers are different from Table 1 because we exclude from Figures 8 and 9 sprites for which an electric field change signature is available, but a reasonably-accurate simulation fit could not be made (i.e., with $R^2 > 0.7$).

The are two key takeaways from Figure 9. First, the jump in median current moment magnitude is larger from columns to carrots, than from carrots to jellyfish. This fact indicates that the determining feature in creating large source current moments is the presence of upward streamers. Second, large and vigorously-luminous sprites have stronger current moments, therefore making these easily-identifiable optical characteristics a proxy for the energetic impacts of sprites in the mesosphere (da Silva & Pasko, 2014; Farges et al., 2005; Sentman et al., 2008). Also note that sprites that were detected exclusively by LEFA (shown in the undetermined category) have large peak current moments, making this group probably a mix of carrots and jellyfish. In other words, sprites that can potentially have a large impact in the mesosphere can easily be detected solely with radio remote sensing.

Our conclusions do not align precisely with the idea put forward by Cummer (2003) who suggested that sprite current signatures are associated only with events with upward streamers. In fact, in our data set we find that column sprites consisting of only downward streamers may also present current signatures, but that they tend to be substantially weaker than in carrot or jellyfish sprites that contain upward streamer development. In Figure 1b, we see that the current moment growth correlates with the sprite optical growth, mostly due to streamer expansion and branching, both down and upward. The peak current moment happens roughly at the same time as peak brightness, dominated by the luminosity of glowing structures inside existing streamer channels. This is in agreement with Cummer, Frey, et al. (2006), who stated that sprite current flows most strongly during subsequent brightening of the sprite, and not during initial downward streamer motion. The uniform luminosity decay shown in Figure 1g, correlated with the current moment reduction, is in alignment with the conclusions of Luque et al. (2016) that distant points within a channel decay at the same rate despite considerable differences in the underlying air density and electrical conductivity.

4 Summary and Conclusions

In this study, we have reported a large number of electromagnetic sprite current signatures obtained in just two consecutive nights of observations. In this data set, we've found that a large fraction of the detected sprites exhibited a current signature. This fraction of 56% is substantially larger than the 10% found in the literature. Moreover, the sprite currents registered in this study are some of the strongest ever reported, with range-normalized electric field changes that have around half the amplitude of its parent flash's, amounting to peak current moments of up to 2,700 kA km. Comparison between optical and electromagnetic properties reveals that carrot and jellyfish sprites (the ones that contain both downward and upward streamers) tend to have larger peak current moments than column sprites (with only downward streamers). We actually see an increasing trend in peak current moment with increasing morphological complexity, from columns to carrots to jellyfish. Thus, we can state that optically-larger sprites also deposit more energy in the mesosphere. Future research will involve determining whether intense sprite currents are a common feature from storms in northwest Texas, and what would be the potential reason. Further research will also help clarify the relationship between sprite current and the interplay of intricate streamer dynamics and the longer lasting sprite glows and beads.

Acknowledgments

This work has been supported by the NSF EPSCoR Program under award OIA-1757207, by NSF award AGS-1917069, and by collaborative grants from Vaisala and Earth Networks. M.G. McHarg is supported by the Air Force Office of Scientific Research. We also thank Earth Networks for making ENTLN pulse data readily available. Data is publicly available at (Contreras-Vidal et al., 2020).

References

Boccippio, D. J., Williams, E. R., Heckman, S. J., Lyons, W. A., Baker, I. T., & Boldi, R. (1995). Sprites, ELF transients, and positive ground strokes. *Science*, *269*, 1088–1091. doi: 10.1126/science.269.5227.1088

Contreras-Vidal, L., Sonnenfeld, R. G., da Silva, C. L., McHarg, M., Jensen, D., Harley, J., … Stenbaek-Nielsen, H. (2020). *Data used in Relationship between sprite current and morphology.* Zenodo, Dataset. Retrieved from `https://doi.org/10.5281/zenodo.4268390` (Available at: https://doi.org/10.5281/zenodo.4268390) doi: 10.5281/zenodo.4268390

Cummer, S. A. (2003). Current moment in sprite-producing lightning. *J. Atmos. Solar-Terr. Phys.*, *65*(5), 499-508. doi: 10.1016/S1364-6826(02)00318-8

Cummer, S. A., Frey, H. U., Mende, S. B., Hsu, R.-R., Su, H.-T., Chen, A. B., …

Takahashi, Y. (2006). Simultaneous radio and satellite optical measurements of high-altitude sprite current and lightning continuing current. *Journal of Geophysical Research: Space Physics*, *111*(A10). Retrieved from `https://agupubs.onlinelibrary.wiley.com/doi/abs/10.1029/2006JA011809` doi: 10.1029/2006JA011809

Cummer, S. A., & Fllekrug, M. (2001). Unusually intense continuing current in lightning produces delayed mesospheric breakdown. *Geophysical Research Letters*, *28*(3), 495-498. Retrieved from `https://agupubs.onlinelibrary.wiley.com/doi/abs/10.1029/2000GL012214` doi: 10.1029/2000GL012214

Cummer, S. A., Inan, U. S., Bell, T. F., & Barrington-Leigh, C. P. (1998). ELF radiation produced by electrical currents in sprites. *Geophys. Res. Lett.*, *25*(8), 1281–1284. doi: 10.1029/98GL50937

Cummer, S. A., Jaugey, N., Li, J., Lyons, W. A., Nelson, T. E., & Gerken, E. A. (2006). Submillisecond imaging of sprite development and structure. *Geophysical Research Letters*, *33*(4). Retrieved from `https://agupubs.onlinelibrary.wiley.com/doi/abs/10.1029/2005GL024969` doi: 10.1029/2005GL024969

Cummer, S. A., & Stanley, M. (1999). Submillisecond resolution lightning currents and sprite development: Observations and implications. *Geophysical Research Letters*, *26*(20), 3205-3208. Retrieved from `https://agupubs.onlinelibrary.wiley.com/doi/abs/10.1029/1999GL003635` doi: 10.1029/1999GL003635

da Silva, C. L., Merrill, R. A., & Pasko, V. P. (2016). Mathematical constraints on the use of transmission line models to investigate the preliminary breakdown stage of lightning flashes. *Radio Sci.*, *51*(5), 367–380. doi: 10.1002/2015RS005853

da Silva, C. L., & Pasko, V. P. (2014). Infrasonic acoustic waves generated by fast air heating in sprite cores. *Geophys. Res. Lett.*, *41*(5), 1789–1795. doi: 10.1002/2013GL059164

da Silva, C. L., & Pasko, V. P. (2015). Physical mechanism of initial breakdown pulses and narrow bipolar events in lightning discharges. *J. Geophys. Res.*, *120*(10), 4989–5009. doi: 10.1002/2015JD023209

da Silva, C. L., & São Sabbas, F. T. (2013). Consequences of the application of the streamer fluid model to the study of the sprite inception mechanism. *Adv. Space Res.*, *51*(10), 1902–1915. doi: 10.1016/j.asr.2012.11.025

Farges, T., Blanc, E., Pichon, A. L., Neubert, T., & Allin, T. H. (2005). Identification of infrasound produced by sprites during the Sprite2003 campaign. *Geophys. Res. Lett.*, *32*. doi: 10.1029/2004GL021212

Franz, R. C., Nemzek, R. J., & Winckler, J. R. (1990). Television image of a large upward electrical discharge above a thunderstorm system. *Science*, *249*, 448–451. doi: 10.1126/science.249.4964.48

Gamerota, W. R., Cummer, S. A., Li, J., Stenbaek-Nielsen, H. C., Haaland, R. K., & McHarg, M. G. (2011). Comparison of sprite initiation altitudes between observations and models. *Journal of Geophysical Research: Space Physics*, *116*(A2). Retrieved from `https://agupubs.onlinelibrary.wiley.com/doi/abs/10.1029/2010JA016095` doi: 10.1029/2010JA016095

Hager, W. W., Sonnenfeld, R. G., Feng, W., Kanmae, T., Stenbaek-Nielsen, H. C., McHarg, M. G., ... Lapierre, J. L. (2012). Charge rearrangement by sprites over a north Texas mesoscale convective system. *J. Geophys. Res.*, *117*. doi: 10.1029/2012JD018309

Heidler, F. (1985). Traveling current source model for LEMP calculation. In *Proc. 6th int. zurich symp. electromagnetic compatibility* (pp. 157–162). Zurich, Switzerland.

Hu, W., Cummer, S. A., & Lyons, W. A. (2007). Testing sprite initiation theory using lightning measurements and modeled electromagnetic fields. *Journal of Geophysical Research: Atmospheres*, *112*(D13). Retrieved from `https://`

agupubs.onlinelibrary.wiley.com/doi/abs/10.1029/2006JD007939 doi: 10.1029/2006JD007939

Hu, W., Cummer, S. A., Lyons, W. A., & Nelson, T. E. (2002). Lightning charge moment changes for the initiation of sprites. *Geophysical Research Letters*, *29*(8), 120-1-120-4. Retrieved from https://agupubs.onlinelibrary.wiley.com/doi/abs/10.1029/2001GL014593 doi: 10.1029/2001GL014593

Lapierre, J. (2019). Earth networks lightning performance in: International conference on lightning and static electricity. Wichita, Kansas, USA.

Li, J., & Cummer, S. (2011). Estimation of electric charge in sprites from optical and radio observations. *Journal of Geophysical Research: Space Physics*, *116*(A1). Retrieved from https://agupubs.onlinelibrary.wiley.com/doi/abs/10.1029/2010JA015391 doi: 10.1029/2010JA015391

Li, J., Cummer, S. A., Lyons, W. A., & Nelson, T. E. (2008). Coordinated analysis of delayed sprites with high-speed images and remote electromagnetic fields. *Journal of Geophysical Research: Atmospheres*, *113*(D20). Retrieved from https://agupubs.onlinelibrary.wiley.com/doi/abs/10.1029/2008JD010008 doi: 10.1029/2008JD010008

Lu, G., Cummer, S. A., Li, J., Zigoneanu, L., Lyons, W. A., Stanley, M. A., ... Samaras, T. (2013). Coordinated observations of sprites and in-cloud lightning flash structure. *Journal of Geophysical Research: Atmospheres*, *118*(12), 6607-6632. Retrieved from https://agupubs.onlinelibrary.wiley.com/doi/abs/10.1002/jgrd.50459 doi: 10.1002/jgrd.50459

Luque, A., & Ebert, U. (2010). Sprites in varying air density: Charge conservation, glowing negative trails and changing velocity. *Geophys. Res. Lett.*, *37*. doi: 10.1029/2009GL041982

Luque, A., Stenbaek-Nielsen, H. C., McHarg, M. G., & Haaland, R. K. (2016). Sprite beads and glows arising from the attachment instability in streamer channels. *Journal of Geophysical Research: Space Physics*, *121*(3), 2431-2449. Retrieved from https://agupubs.onlinelibrary.wiley.com/doi/abs/10.1002/2015JA022234 doi: 10.1002/2015JA022234

Marshall, R. A. (2012). An improved model of the lightning electromagnetic field interaction with the D-region ionosphere. *J. Geophys. Res.*, *117*. doi: 10.1029/2011JA017408

Marshall, R. A., da Silva, C. L., & Pasko, V. P. (2015). Elve doublets and compact intracloud discharges. *Geophys. Res. Lett.*, *42*(14), 6112–6119. doi: 10.1002/2015GL064862

Nag, A., Rakov, V. A., & Cummins, K. L. (2014). Positive lightning peak currents reported by the u.s. national lightning detection network. *IEEE Transactions on Electromagnetic Compatibility*, *56*(2), 404-412.

Orville, R. E. (1991). Calibration of a magnetic direction finding network using measured triggered lightning return stroke peak currents. *J. Geophys. Res.*, *96*(D9), 17135–17142. doi: 10.1029/91JD00611

Pasko, V. P. (2010). Recent advances in theory of transient luminous events. *J. Geophys. Res.*, *115*. doi: 10.1029/2009JA014860

Pasko, V. P., Inan, U. S., Bell, T. F., & Reising, S. C. (1998). Mechanism of ELF radiation from sprites. *Geophys. Res. Lett.*, *25*(18), 3493–3496. doi: 10.1029/98GL02631

Pasko, V. P., Inan, U. S., Bell, T. F., & Taranenko, Y. N. (1997). Sprites produced by quasi-electrostatic heating and ionization in the lower ionosphere. *J. Geophys. Res.*, *102*(A3), 4529–4561. doi: 10.1029/96JA03528

Rakov, V. A., & Uman, M. A. (1998). Review and evaluation of lightning return stroke models including some aspects of their application. *IEEE Trans. Electromag. Compat.*, *40*(4), 403-426. doi: 10.1109/15.736202

Reising, S. C., Inan, U. S., & Bell, T. F. (1999). Elf sferic energy as a proxy indicator for sprite occurrence. *Geophysical Research Letters*, *26*(7), 987-990.

Retrieved from https://agupubs.onlinelibrary.wiley.com/doi/abs/10.1029/1999GL900123 doi: 10.1029/1999GL900123

Sentman, D. D., Stenbaek-Nielsen, H. C., McHarg, M. G., & Morrill, J. S. (2008). Plasma chemistry of sprite streamers. *J. Geophys. Res.*, *113*. doi: 10.1029/2007JD008941

Sentman, D. D., Wescott, E. M., Osborne, D. L., Hampton, D. L., & Heavner, M. J. (1995). Preliminary results from the Sprites94 aircraft campaign: 1. Red sprites. *Geophys. Res. Lett.*, *22*(10), 1205–1208. doi: 10.1029/95GL00583

Sonnenfeld, R. G., & Hager, W. W. (2013). Electric field reversal in sprite electric field signature. *Mon. Weather Rev.*, *141*, 1731–1735. doi: 10.1175/MWR-D-12-00220.1

Soula, S., Defer, E., Fllekrug, M., van der Velde, O., Montanya, J., Bousquet, O., … Pedeboy, S. (2015). Time and space correlation between sprites and their parent lightning flashes for a thunderstorm observed during the hymex campaign. *Journal of Geophysical Research: Atmospheres*, *120*(22), 11,552-11,574. Retrieved from https://agupubs.onlinelibrary.wiley.com/doi/abs/10.1002/2015JD023894 doi: 10.1002/2015JD023894

Soula, S., Van der Velde, O., Montany, J., Neubert, T., Chanrion, O., & Ganot, M. (2009). Analysis of thunderstorm and lightning activity associated with sprites observed during the eurosprite campaigns: Two case studies. *Atmospheric Research*, *91*, 514-528. doi: 10.1016/j.atmosres.2008.06.017

Stanley, M., Brook, M., Krehbiel, P., & Cummer, S. A. (2000). Detection of daytime sprites via a unique sprite elf signature. *Geophysical Research Letters*, *27*(6), 871-874. Retrieved from https://agupubs.onlinelibrary.wiley.com/doi/abs/10.1029/1999GL010769 doi: 10.1029/1999GL010769

Stenbaek-Nielsen, H. C., & McHarg, M. G. (2008). High time-resolution sprite imaging: observations and implications. *J. Phys. D: Appl. Phys.*, *41*. doi: 10.1088/0022-3727/41/23/234009

Uman, M. A., & McLain, D. K. (1969). Magnetic field of lightning return stroke. *J. Geophys. Res.*, *74*(28), 6899–6910. doi: 10.1029/JC074i028p06899

Uman, M. A., McLain, D. K., & Krider, E. P. (1975). The electromagnetic radiation from a finite antenna. *Am. J. Phys.*, *43*(1), 33–38. doi: 10.1119/1.10027

Wait, J. R., & Spies, K. P. (1964). *Characteristics of the Earth-ionosphere waveguide for VLF radio waves* (Vol. 13; Tech. Rep. No. 300). Natl. Bur. of Stand., Boulder, Co.

Zhang, J. (2010). Development and test of the langmuir electric field array master's. *Thesis. New Mexico Institue of Mining and Technology.*

Zhu, Y., Rakov, V. A., Tran, M. D., Stock, M. G., Heckman, S., Liu, C., … Hare, B. M. (2017). Evaluation of entln performance characteristics based on the ground truth natural and rocket-triggered lightning data acquired in florida. *Journal of Geophysical Research: Atmospheres*, *122*(18), 9858-9866. Retrieved from https://agupubs.onlinelibrary.wiley.com/doi/abs/10.1002/2017JD027270 doi: 10.1002/2017JD027270